Multi-scale microscopy study of 3D morphology and structure of MoNi$_4$/MoO$_2$@Ni electrocatalytic systems for fast water dissociation

Ehrenfried Zschech [a,b,*], Emre Topal [c,d,1], Kristina Kutukova [c,2], Jürgen Gluch [c,3], Markus Löffler [d], Stephan Werner [e], Peter Guttmann [e], Gerd Schneider [e,f], Zhongquan Liao [c], Janis Timoshenko [g]

[a] deepXscan GmbH, Dresden, Germany
[b] Faculty of Chemistry, University of Warsaw, Warsaw, Poland
[c] Fraunhofer Institute for Ceramic Technologies and Systems, Dresden, Germany
[d] Dresden Center for Nanoanalysis, Center for Advancing Electronics Dresden, Technische Universität Dresden, Dresden, Germany
[e] Helmholtz-Zentrum Berlin, Berlin, Germany
[f] Institut für Physik, Humboldt-Universität zu Berlin, Berlin, Germany
[g] Interface Science Department, Fritz Haber Institute of Max Planck Society, Berlin, Germany

ARTICLE INFO

ABSTRACT

The 3D morphology of hierarchically structured electrocatalytic systems is determined based on multi-scale X-ray computed tomography (XCT), and the crystalline structure of electrocatalyst nanoparticles is characterized using transmission electron microscopy (TEM), supported by X-ray diffraction (XRD) and spatially resolved near-edge X-ray absorption fine structure (NEXAFS) studies. The high electrocatalytic efficiency for hydrogen evolution reaction (HER) of a novel transition-metal-based material system – MoNi$_4$ electrocatalysts anchored on MoO$_2$ cuboids aligned on Ni foam (MoNi$_4$/MoO$_2$@Ni) – is based on advantageous crystalline structures and chemical bonding. High-resolution TEM images and selected-area electron diffraction patterns are used to determine the crystalline structures of MoO$_2$ and MoNi$_4$. Multi-scale XCT provides 3D information of the hierarchical morphology of the MoNi$_4$/MoO$_2$@Ni material system nondestructively: Micro-XCT images clearly resolve the Ni foam and the attached needle-like MoO$_2$ micro cuboids. Laboratory nano-XCT shows that the MoO$_2$ micro cuboids with a rectangular cross-section of $0.5 \times 1 \ \mu m^2$ and a length of 10–20 μm are vertically arranged on the Ni foam. MoNi$_4$ nanoparticles with a size of 20–100 nm, positioned on single MoO$_2$ cuboids, were imaged using synchrotron radiation nano-XCT. The application of a deep convolutional neural network (CNN) significantly improves the reconstruction quality of the acquired data.

1. Introduction

A systematic materials selection and the synthesis of high-performance and low-cost non-precious metal catalysts for electrochemical energy conversion can only be based on establishing a general relationship between physicochemical properties of the materials and the electrocatalytic performance and stability of the system. The design of highly performant and durable 3D electrocatalytic systems requires surface structures with high activity and an optimized hierarchical morphology (Topal, Liao, et al., 2020).

The activity of materials for electrochemical energy conversion is usually discussed based on their crystalline structure and chemical bonding. X-ray diffraction (XRD) and transmission electron microscopy (TEM) as well as X-ray photon spectroscopy (XPS) and sometimes X-ray absorption spectroscopy (XAS) are analytical techniques that provide the respective information on "atomic level". The total surface area of the electrocatalytic active material and the fluid-dynamic processes depend on the morphology of the formed nanostructures. Detailed 3D

information about the morphology of the advanced electrocatalytically active materials can be derived from tomography studies. Depending on the typical size of the studied objects, electron tomography (ET) in the TEM or X-ray computed tomography (XCT), both nano-XCT and micro-XCT, are suitable techniques to provide the morphology of the (sub-) structures of the hierarchical materials. Both the intrinsic activity of the electrocatalytic material and the number of active sites, given by the morphology, are essential parameters for the operational performance and the stability of the whole electrocatalytic system.

Because of their unique electronic properties and anticipated synergetic effects to alter significantly surface properties of materials, Ni and Mo are potential constituents for electrocatalytic materials. Ni atoms are characterized by a high reactivity and Mo atoms have superior adsorption properties towards hydrogen. Studies of Ni- or Mo-based electrocatalysts have been reviewed recently (Vij et al., 2017). Many of them have shown promising electrocatalytic activity for hydrogen evolution reaction (HER). Particularly, reactivity and hydrogen adsorption are high for Mo_xNi_y-based electrocatalysts (Zhang et al., 2017). The high electrocatalytic efficiency of Mo_xNi_y electrocatalysts is based on their advantageous surface chemistry, i.e., the crystalline structure of the materials and the chemical bonding. In addition to the intrinsic properties of the constituent components, the 3D morphology of electrocatalysts has to be tailored, as it is closely related to the exposed facets and active sites (Xu et al., 2015; Liu and Li, 2016; Hao et al., 2015). The design of electrocatalytic systems with an optimized hierarchical morphology and surface structures with high activity, resulting in highly performant and durable systems, is a task that is expected to play an increasing role in the future (Zhang et al., 2018).

The objective of this study is to determine the 3D morphology of a novel, hierarchically structured transition-metal-based materials system – $MoNi_4$ electrocatalysts anchored on MoO_2 cuboids aligned on Ni foam ($MoNi_4/MoO_2@Ni$) – based on multi-scale X-ray computed tomography (XCT) and to characterize the crystalline structure of electrocatalyst nanoparticles using X-ray diffraction (XRD), near-edge X-ray absorption fine structure (NEXAFS) studies and transmission electron microscopy (TEM). The application of artificial intelligence (AI) algorithms significantly is used to improve the quality of the acquired tomography and spectromicroscopy data.

2. Materials and methods

2.1. Synthesis of the $MoNi_4/MoO_2@Ni$ material system

A novel platinum-free electrocatalyst explored for hydrogen evolution reaction (HER) in alkaline solution was studied: $MoNi_4$ electrocatalyst nanoparticles anchored on MoO_2 cuboids that were aligned on conductive Ni foam ($MoNi_4/MoO_2@Ni$). The synthesis of the $MoNi_4$ electrocatalyst nanoparticles involved two steps (Zhang et al., 2017). Firstly, $NiMoO_4$ cuboids were grown on a piece of Ni foam (1×3 cm^2) during a hydrothermal synthesis in a drying oven at 150 °C for 6 h in 15 ml deionized water containing $Ni(NO_3)_2 \cdot 6H_2O$ (0.04 M) and $(NH_4)_6Mo_7O_{24} \cdot 4H_2O$ (0.01 M) in a Teflon autoclave. The coordination of Mo^{6+} ions of the precursor cuboids is octahedral in the α-$NiMoO_4$ phase while it is tetrahedral in both the β-$NiMoO_4$ phase and the $NiMoO_4 \bullet nH_2O$ phase (Rodriguez et al., 1998). The crystalline structure of the α-$NiMoO_4$ cuboids was proven by X-ray diffraction (XRD), see XRD pattern in Fig. 1a. Secondly, $MoNi_4$ nanoparticles on the surface of the cuboids were formed by controlling the outward diffusion of nickel atoms during annealing of the precursor $NiMoO_4$ cuboids (Topal, Liao, et al., 2020; Zhang et al., 2017). While the as-synthesized $NiMoO_4$ cuboids were heated in a H_2/Ar (4/96 vol%) atmosphere at 500 °C for 2 h, Ni atoms diffused in a controlled way to the surface of the cuboids and formed numerous $MoNi_4$ nanoparticles with a size of 20–100 nm on the surface of the MoO_2 cuboids. The XRD pattern in Fig. 1b confirms the formation of MoO_2. That means, the composition of the cuboids changed from $NiMoO_4$ to MoO_2 caused by Ni out-diffusion. While MoO_3 – a wide band gap semiconductor – is electrically insulating, MoO_2 is electrically conductive (Scanlon et al., 2010; Inzani et al., 2017). The MoO_6 octahedrons in MoO_2 show a distortion with Mo—O bond lengths in the 1.97–2.07 Å range (A. Bolzan et al., 1995; Lajaunie et al., 2015). The data indicate that H_2 is a key parameter for the formation of the $MoNi_4/MoO_2@Ni$ material system (Zhang et al., 2017).

The resulting hierarchically structured materials exhibit electrocatalytically active $MoNi_4$ nanoparticles anchored on MoO_2 cuboids that are vertically aligned on the conductive Ni foam. A scheme is shown in Fig. 2 (Topal, Liao, et al., 2020).

2.2. Micro-XCT (laboratory tool)

The micro-XCT data acquisition was performed using a Carl Zeiss Versa 520 tool. The micro-XCT system uses a cone-beam geometry with a fixed horizontal optical axis and a vertical sample rotation axis (Fig. 3). As for all cone-beam XCT systems, the geometric magnification is given by Thales' intercept theorem, i.e., the magnification is defined as the ratio of the source-detector distance to the source-object-distance. Consequently, since the latter one is restricted by the object diameter, and the object-detector distance is restricted by the size of the tool itself, a sample-size-dependent limit on geometric magnification is imposed. To circumvent this restriction, the Carl Zeiss Versa 520 tool employs an additional optical magnification stage. The detector of a conventional XCT system is replaced by a thin, fine-grained, optically transparent scintillator film positioned in the focal point of an objective for visible
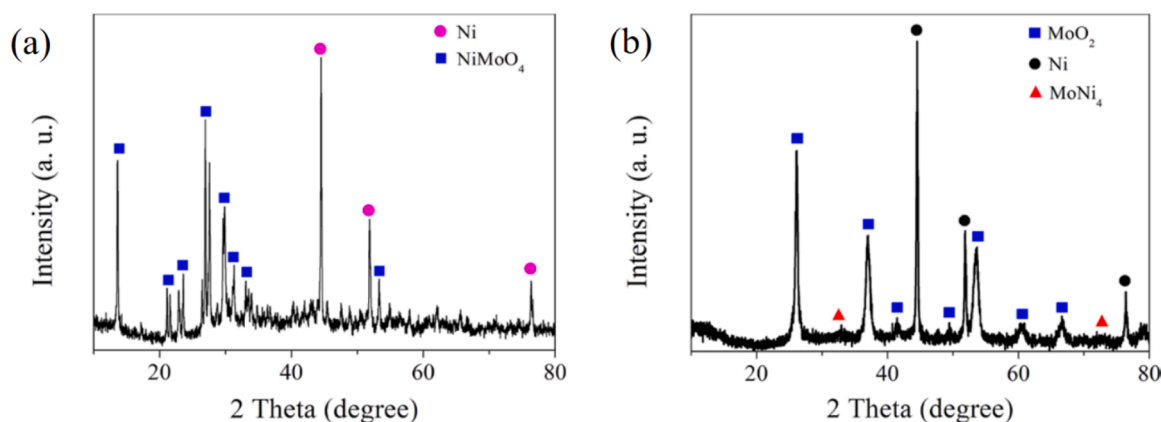

Fig. 1. XRD patterns (Cu-Kα radiation) of (a) $NiMoO_4$ cuboids on the nickel foam and (b) $MoNi_4/MoO_2@Ni$, synthesized at 500 °C for 2 h in H_2/Ar atmosphere (Ni: JCPDS, No. 65-2865; metallic MoO_2: JCPDS, No. 32-0671; $MoNi_4$: JCPDS, No. 03-1036). XRD patterns were recorded on a PW1820 powder diffractometer (Phillips) using Cu-Kα radiation. Figure based on Zhang et al. (2017).
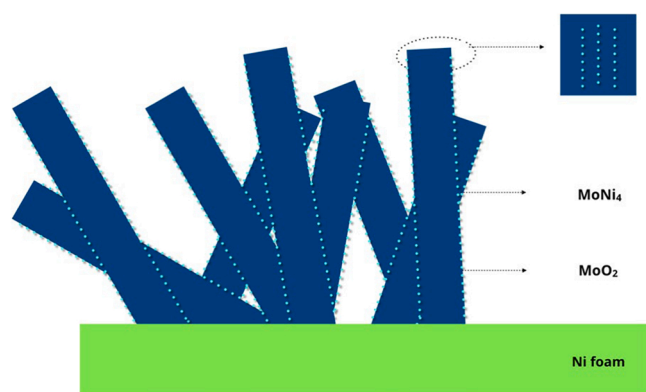
Fig. 2. The hierarchical structure of the studied electrocatalyst system: $MoNi_4$ electrocatalysts anchored on MoO_2 cuboids aligned on conductive Ni foam, based on transmission X-ray microscopy and scanning electron microscopy images (Topal, Liao, et al., 2020; Zhang et al., 2017).

light. The image produced by the geometric magnification of the conventional XCT part is further optically magnified onto a sensitive $2k \times 2k$ optical CCD camera with only 13.5 μm pixel size. Since the total magnification is given by the product of geometrical and optical magnifications, high magnification can be achieved even for larger objects.

The sample for the micro-XCT study was prepared by picking up a loose particle from a section of the Ni support foam with MoO_2 cuboids and $MoNi_4$ electrocatalysts on it, and subsequently, it was fixed on the sample holder. The sample size was about $377 \times 590 \times 365$ μm^3. An X-ray tube with source filter LE4 was operated at a voltage of 80 kV to enable optimal transmission and contrast, and the power was set to the maximum value of 7 W. The scan parameters were set to a voxel size of 0.448 μm, employing a geometric magnification of 1.5 and an optical

magnification of 20. A tilt series with 2401 projections, satisfying the requirements of Nyquist sampling, was recorded for a complete rotation (angular range 360°). The exposure time per image was 30 s.

2.3. Nano-XCT (laboratory tool)

The nano-XCT data acquisition was performed using a Xradia nano-XCT 100 tool equipped with a rotating anode X-ray source (Cu-Kα radiation, 8 keV photon energy). Fig. 4 shows the scheme of the X-ray microscope used. In contrast to the cone-beam geometry of the conventional micro-XCT, X-ray microscopy setups offer a (nearly) parallel-beam imaging. Therefore, an angular range of 180° is sufficient for the acquisition of the tomography data. Laboratory X-ray microscopes operated in the multi-keV range use Fresnel zone plates as focusing objective lenses, that are limiting the spatial resolution of the microscope to about 50 nm. The enlarged image is projected onto a thin scintillator and subsequently recorded by an optical microscope with a CCD camera.

A MoO_2 cuboid sample with a size of about $15 \times 15 \times 15$ μm^3 was picked up from the Ni foam and fixed on the tip of a tungsten wire. The laboratory nano-XCT studies were performed in high resolution mode ($40 \times$ FZP magnification $\times 20 \times$ optical magnification $= 800 \times$ total magnification). The field of view width and height were 16 μm with 512 pixels for each, resulting in a voxel size of 31 nm. The tilt series for the tomography consisted of 501 images within an angular range of 180°. The exposure time per image was 265 s

2.4. Nano-XCT and NEXAFS (synchrotron radiation beamline)

The synchrotron radiation nano-XCT data were recorded at the collimated plane grating monochromator (PGM) beamline at the undulator U41 at BESSY-II in the soft X-ray and in the tender X-ray range
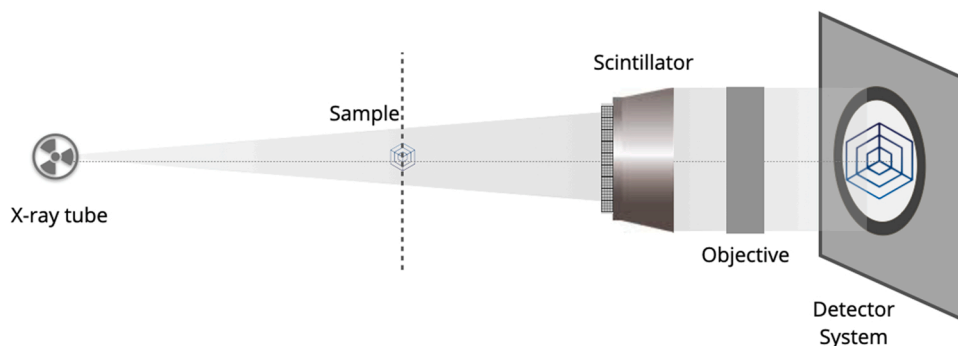

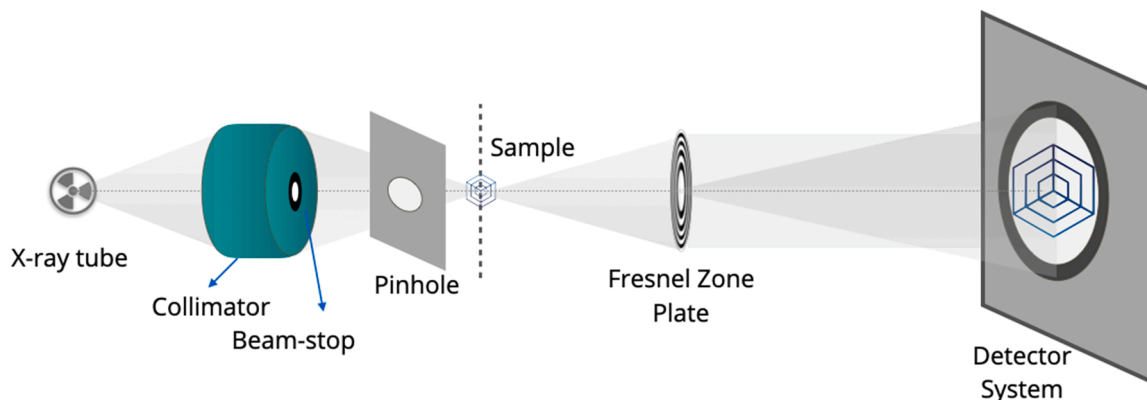**Fig. 3.** Cone-beam geometry as characteristic for a micro-XCT setup.

Fig. 4. Nearly parallel-beam geometry as characteristic for a nano-XCT setup.

up to a photon energy of about 3.0 keV (see Fig. 5). The X-ray microscope for spectromicroscopy experiments, that allows imaging with high spatial resolution and local near-edge X-ray absorption fine structure (NEXAFS) studies, is located in 9 m distance from the exit slit of the PGM.

The sample with a size of about $2.4 \times 0.4 \times 0.2\ \mu m^3$ was cleaned in an ultrasonic bath in ethanol, and subsequently, it was dipped on a quantifoil TEM grid. The spatial resolution of the synchrotron radiation nano-XCT tool was 36 nm, and the achieved voxel size was 9.4 nm. Due to the sample geometry, the tomography tilt series was limited to 110°, with 111 individual images. The exposure time per image was 2 s. The NEXAFS spectra were recorded in the vicinity of the Mo-L absorption edges.

2.5. HR-TEM

The sample was sliced by a razor blade, and powders were collected by a lacey TEM grid. Thin edges were selected in the TEM for high-resolution transmission electron microscopy (HR-TEM). HR-TEM studies were performed using a Carl Zeiss LIBRA 200 MC Cs scanning TEM tool operating at an acceleration voltage of 200 kV. Energy-dispersive X-ray spectroscopy (EDX) was performed on the samples using a detector of Oxford Instruments attached to the TEM.

2.6. Image reconstruction, advanced image data analysis and NEXAFS data processing

A novel hybrid tomographic image reconstruction approach was developed and implemented for parallel-beam and cone-beam geometries (Topal, Loeffler, et al., 2020) (see Figs. 6–8). The acquired projection data from micro-XCT, laboratory nano-XCT and synchrotron radiation nano-XCT were reconstructed using the Feldkamp-Davis-Kress (FDK) (Feldkamp et al., 1984) and the Filtered-Back-Projection (FBP) (Radon, 1986) reconstruction algorithms for cone-beam and parallel-beam projection, respectively. The size of the reconstructed volume was 1994^3 voxels (voxel size 0.44 μm) for the micro-XCT data, 512^3 voxels (voxel size 31.9 nm) for the laboratory nano-XCT data and 541^3 voxels (voxel size 9.4 nm) for the synchrotron radiation nano-XCT data. The hybrid approach includes data driven and machine learning approaches for the suppression of artifacts in combination with an analytic image reconstruction algorithm. The workflow of the reconstruction procedure for multi-scale XCT data is explained in Topal, Liao et al. (2020), Fig. 9 and Topal, Loeffler et al. (2020). After normalization of the intensities of the acquired raw radiographs and an intensity adjustment to improve the contrast – as a part of the beam hardening correction – several sources for inaccuracy and image artefacts were eliminated or at least mitigated before the reconstruction process: offsets of the object's center of rotation and of the detector positioning. To correct object motion, computer vision and deep neural network approaches were combined to adapt feature tracking to the acquisition procedure of computed tomography data where the features are changing over angles. The applied correction algorithms do not depend on the studied sample volume and the resolution, they are identically for the analysis of the data from micro-XCT, laboratory nano-XCT and synchrotron radiation nano-XCT. Subsequently, the processed reconstructed data were transferred and segmented using the Simpleware ScanIp software (Synopsys Inc., Mountain View, CA, USA) (Simpleware ScanIP, 2019). Finally, the segmented 3D data were used to visualize the 3D morphology of the materials system and were converted to a surface mesh for designing a solid geometry using reverse engineering tools available in SpaceClaim (ANSYS Inc., Canonsburg, PA, USA) (ANSYS SpaceClaim, 2019).

For the NEXAFS analysis (Mo L absorption edges), after subtraction of the background $I_0(x, y, E)$ for each pixel of the images, the intensity of transmitted X-rays $I_1(x, y, E)$ was converted into values of X-ray absorption coefficients according to $\mu(x,y,E) = -\log [I_1(x,y,E)/I_0(x,y,E)]$. The background function $\mu_{bg}(x,y,E)$ for each pixel was constructed based on an interpolation of the measured X-ray intensity for the sample regions not covered by the sample. Knowing the background function, the absorption jump value $\Delta\mu(x,y,E) = \mu(x,y,E) - \mu_{bg}(x,y,E)$ was calculated for each pixel. The latter is proportional to the concentration of absorbing Mo atoms in the region. Furthermore, the normalization of NEXAFS spectra was performed by dividing the pixel-specific NEXAFS spectra after background subtraction by the corresponding $\Delta\mu(x,y,E)$ value. The chemically distinct components of a sample were then determined based on a principal component data analysis (PCA) (Wasserman, 1997). For this purpose, the spatially resolved spectra from images for $MoNi_4/MoO_2$ and $NiMoO_4$ samples after background subtraction and normalization were merged in a single dataset, and a PCA was performed by employing the singular value decomposition of the data matrix, as implemented in *Wolfram Mathematica* code. The orthogonal basis vectors yielded by PCA (principal components) were used to reconstruct the original spectra. Only three principal components were needed to reconstruct all NEXAFS spectra corresponding to different pixels of the images. The first component is just a NEXAFS spectrum, averaged over all pixels, and its contribution to all pixel-specific spectra is practically the same (note that the averaged spectrum was not subtracted from the dataset before the singular value decomposition, as sometimes is done in PCA). The weights of the 2nd and 3rd principal components to the pixel-specific NEXAFS spectra, in turn, are different, suggesting that there are, in total, two distinct Mo species present in the samples studied (Mo species in different oxidation states). The weights of these two principal components in the NEXAFS spectra collected at different pixels were used to assign each pixel to one or another Mo species.

3. Results and discussion

3.1. Morphology of the $MoNi_4/MoO_2@Ni$ material system

The hierarchical morphology of the $MoNi_4/MoO_2@Ni$ material system was determined based on experimental data from micro-XCT, laboratory nano-XCT and synchrotron radiation nano-XCT, followed by the advanced 3D reconstruction methodology and AI-based further data
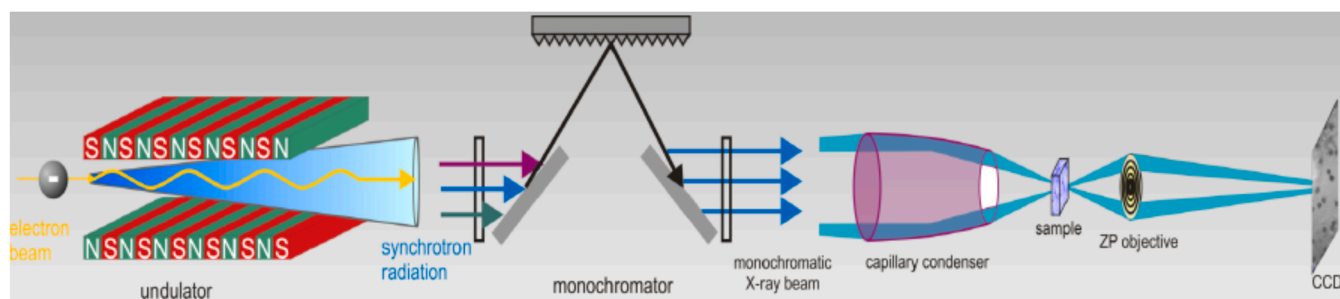

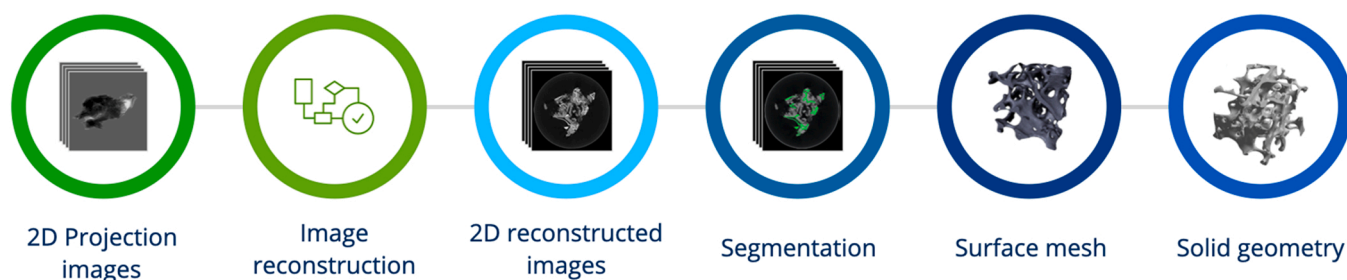**Fig. 5.** Nano-XCT setup at the PGM beamline at the undulator U41 at BESSY-II.

Fig. 6. Data analysis in XCT: from as-recorded 2D image data to an accurate 3D morphology.
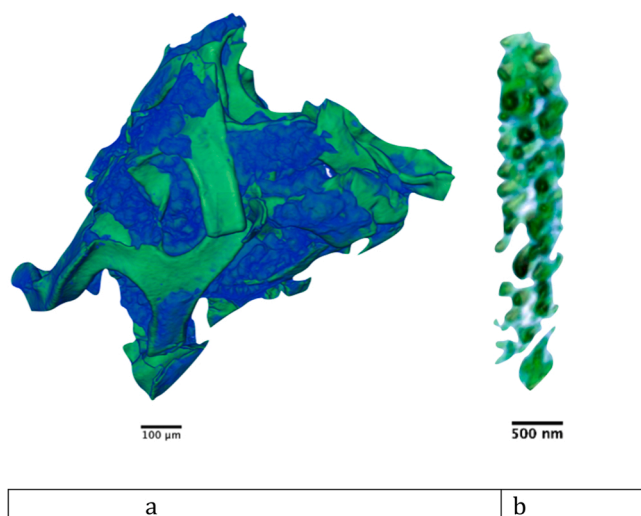

Fig. 7. The reconstructed 3D volume rendering of the MoNi$_4$/MoO$_2$@Ni sample (fully segmented and processed data), (a) from micro-XCT: The MoO$_2$ cuboids on the Ni foam are visualized. Green color is used for the visualization of the Ni foam and blue color for the needle-like MoO$_2$ micro cuboids. (b) from synchrotron radiation nano-XCT: The MoNi$_4$ electrocatalytically active nanosized particles anchored on a single MoO$_2$ micro cuboid are visualized.

analysis as described above, to suppress image artefacts and to improve the image quality. The multi-scale tomography data, analyzed as described above, provide comprehensive 3D information about the hierarchical structure of the studied electrocatalyst system (Zhang et al., 2017): MoNi$_4$ electrocatalysts anchored on MoO$_2$ cuboids aligned on conductive Ni foam.

Fig. 7 provides exemplary reconstructed 3D volume rendering of the MoNi$_4$/MoO$_2$@Ni material system based on XCT data acquired with different spatial resolution, i.e., from micro-XCT and from synchrotron radiation nano-XCT.

The data analysis process flow – according to Fig. 6 – is exemplarily provided for the micro-XCT data of the MoNi$_4$/MoO$_2$@Ni material system in Fig. 8 (for more details see Topal, Liao, et al., 2020). The effect of AI-based correction of unavoidable experimental errors is provided in Fig. 8a and b, while Fig. 8c and d provide a stack of segmented images and the resulting 3D surface mesh. The surface mesh is defined by vertices, edges and either one of polygons or faces. The more complex the morphology is, the more and smaller vertices are needed to close the surface.

Summarizing the experimental micro-XCT and nano-XCT data, the 3D morphology of electrocatalyst supporting structures can be characterized in the following way:

- The micro-XCT images clearly resolve the Ni foam and the attached needle-like MoO$_2$ micro cuboids.

- The MoO$_2$ micro cuboids were imaged using laboratory nano-XCT. The MoO$_2$ micro cuboids are vertically arranged on the Ni foam, and the lengths of these cuboids are in the range of 10–20 μm with a rectangular cross-section of 0.5×1 μm^2.
- MoNi$_4$ nanoparticles positioned on one single MoO$_2$ cuboid were imaged using synchrotron radiation nano-XCT. The MoNi$_4$ nanoparticles are anchored on the MoO$_2$ cuboid. The sizes of these round shaped MoNi$_4$ nanoparticles are in the range of 20–100 nm.

The acquisition of X-ray absorption spectra (XAS) and of electron energy loss spectra (EELS) in the surrounding of absorption edges provides information about the local density of states of the material, in case of spectromicroscopy (using a transmission X-ray microscope or a transmission electron microscope) with high spatial resolution. A limitation for EELS is that the intensity of ionization edges drops with increasing energy loss, and therefore, it's usable energy range is typically below ~ 2 keV (Egerton, 2011). The study of the near edge X-ray absorption fine structure (NEXAFS) around the Mo-L absorption edges is of particular interest for applications in the fields of energy conversion and energy storage, and particularly of the samples studied in this paper.

Since spectromicroscopy at the Mo-L absorption edges (NEXAFS) allows for studying the structure and the chemical bonding of submicron size components of complex materials systems, spatially resolved Mo L$_3$ NEXAFS spectra for two different samples were recorded, for NiMoO$_4$ and for MoO$_2$/MoNi$_4$ (Werner et al., 2022). Fig. 9 presents schematically the image acquisition – spatially resolved intensities of transmitted X-rays for the NiMoO$_4$ sample at several photon energies in the vicinity of the Mo L$_3$ edge and the NEXAFS spectra extracted from the taken energy series at defined sample positions for the NiMoO$_4$ and MoO$_2$/MoNi$_4$ samples. Additional NEXAFS spectra in the vicinity of other X-ray absorption edges are shown and discussed in (Werner et al., 2022).

NEXAFS data from synchrotron-based measurements were used to prove the correct segmentation. was performed based on synchrotron radiation X-ray microscopy images recorded in an energy range around the Mo-L absorption edges. The X-ray microscopy images in Fig. 10 show spatially resolved intensity of transmitted X-rays in the vicinity of Mo-L$_2$ edge for the MoNi$_4$/MoO$_2$ catalyst and for the NiMoO$_4$ precursor. These maps contain 1300×1340 pixels, where the intensity of transmitted X-rays was collected for each pixel at 81 different energies between 2616 and 2640 eV with $\Delta E = 0.3$ eV (results averaged over all energy points are shown in Fig. 10).

After background subtraction and normalization, the spatially resolved spectra from both images were merged in a single dataset, and analyzed using principal component analysis (PCA). PCA revealed that all spectra can be represented as a linear combination of the contributions from only two species. These two species are attributed to different oxidation states of Mo. Distributions of these species can be visualized by plotting the weight of the 2nd principal component to a color code for each pixel (Fig. 10). Here the size of the circle, centered at each of the pixels, corresponds to the concentration of Mo (estimated from the absorption jump value), while the color of the pixel corresponds to the weight of the 2nd principal component. and thus, it is related to different
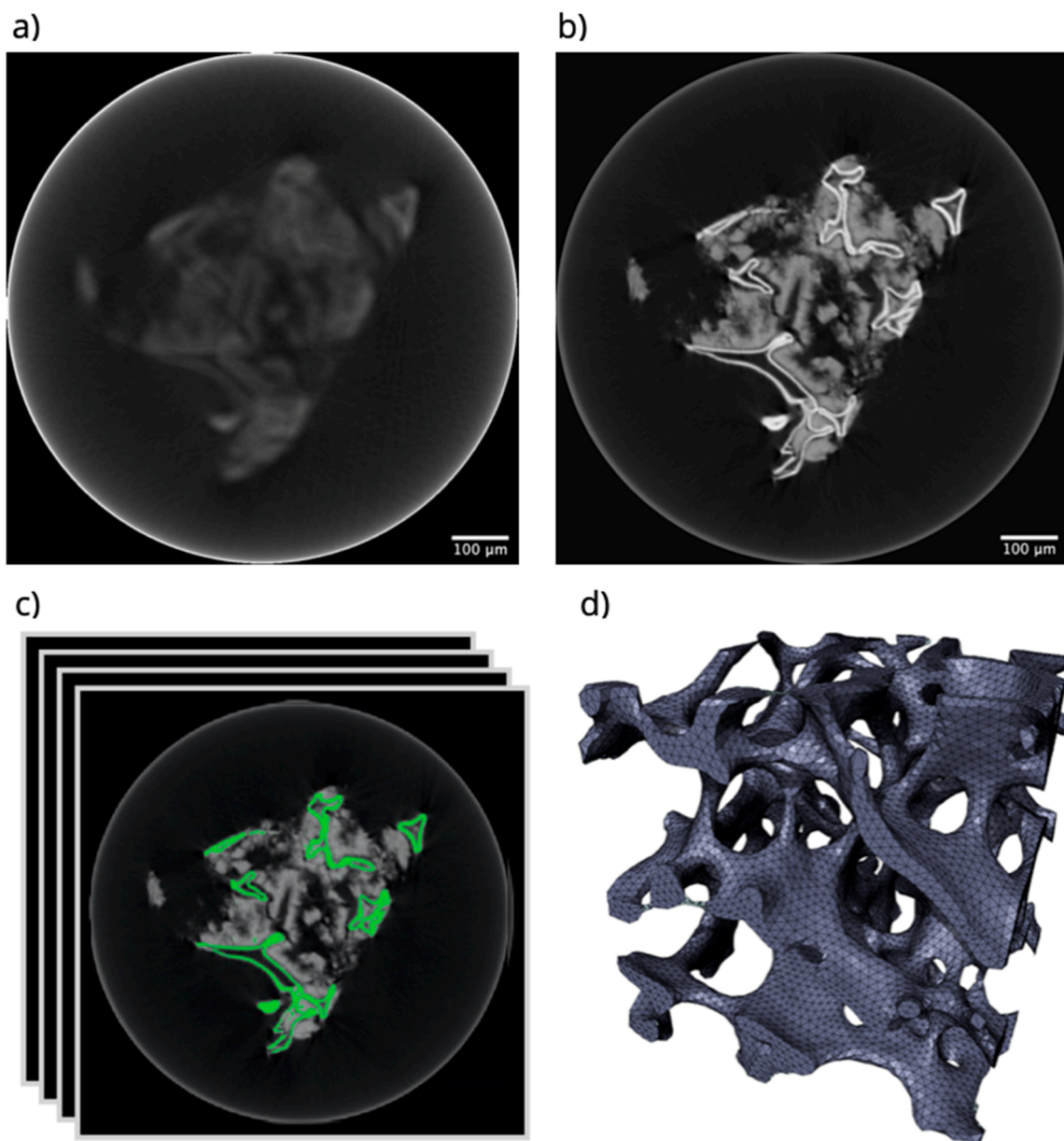
Fig. 8. (a) and (b) One reconstructed virtual cross-section of the MoNi$_4$/MoO$_2$@Ni sample based on micro-XCT data. The hollow white lines are the Ni foam and the grey zones are MoO$_2$ micro cuboids. The MoNi$_4$ nanoparticles are not resolvable in the micro-XCT study. (a) prior to the correction procedure, (b) after the beam-hardening correction/intensity adjustment, detector offset and center of rotation correction, and final motion compensation. (c) stack of segmented images (cross-sections) – green: Ni foam scaffold (see also Fig. 2) –, and (d) resulting 3D surface mesh.

Mo oxidation states. One can observe that the Mo species present in the two samples investigated are clearly different. In particular, the MoNi$_4$/MoO$_2$ sample is dominated by the spectra with negative value of the 2nd principal component weight (red points). In contrast, spectra of the NiMoO$_4$ sample have positive value of the 2nd principal component (blue points) for all pixels. Each sample is dominated by points of only one color, i.e., each sample contains only one Mo oxidation state. The identification of these components is performed below by analyzing representative NEXAFS spectra for each sample (Fig. 9).

Summarizing, based on a detailed principal component analysis on merged datasets (Wasserman, 1997) containing data from all pixels in both samples, we could prove different chemical states for the investigated components in both samples and particularly that the Ni out-diffusion process – and consequently the formation of MoNi$_4$ nanoparticles – was fully completed.

3.2. Structure of the components of the MoNi$_4$/MoO$_2$@Ni material system

High-resolution structure studies of components of the MoNi$_4$/MoO$_2$@Ni material system, particularly of the MoNi4 electrocatalyst, were performed using TEM. The HRTEM images of the samples show lattice fringes with lattice distances of 0.35 and 0.28 nm (Fig. 12 a and b), which correspond to the (110) plane of MoO$_2$ and the (200) plane of MoNi$_4$, respectively. The corresponding elemental maps (Fig. 11 c) indicate that the surface nanoparticles are mainly rich in Ni and Mo (MoNi$_4$ electrocatalysts), and the cuboid contains Mo and O (MoO$_2$ cuboid). The Mo/Ni atomic ratio of 1:3.84 for the nanoparticles, determined with TEM-EDX point analysis and using a standardless data correction mode, indicates the formation of MoNi$_4$ crystals, confirming the XRD results.

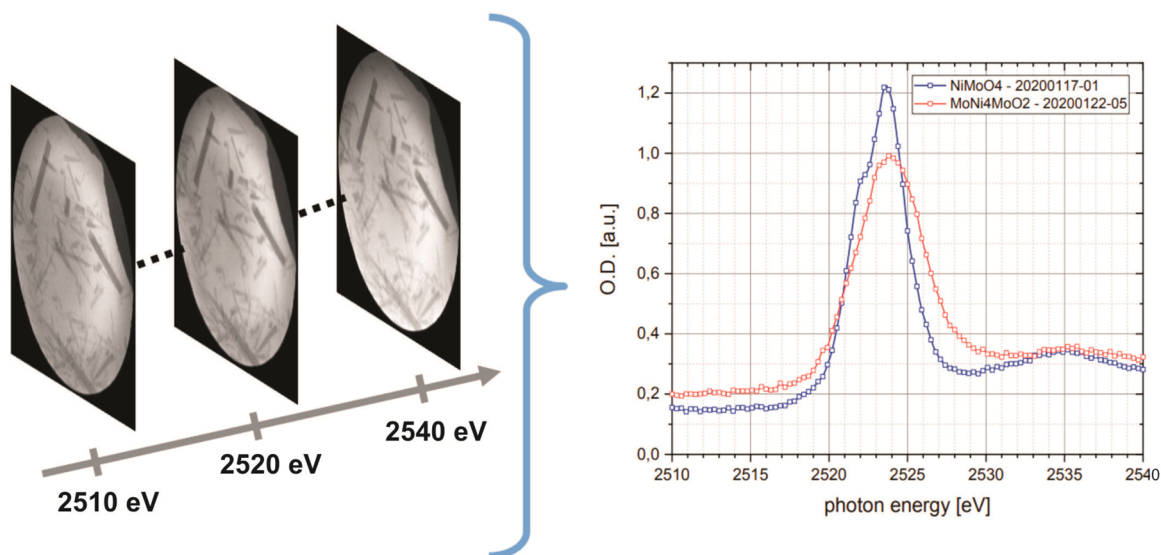As discussed above, PCA analysis shows that the spectra collected for

Fig. 9. Schematic demonstration of the X-ray microscopy image acquisition at several photon energies in the vicinity of the Mo-L_3 edge, and Mo-L_3 NEXAFS spectra of the $NiMoO_4$ and $MoO_2/MoNi_4$ samples. Optical density (O.D.) data were taken with the monochromator using a multilayer optics, exit slit width = 7 µm ($NiMoO_4$) and 5 µm ($MoO_2/MoNi_4$), Fresnel zone plate objective with 25 nm outermost zone width and 2 s exposure time per image.
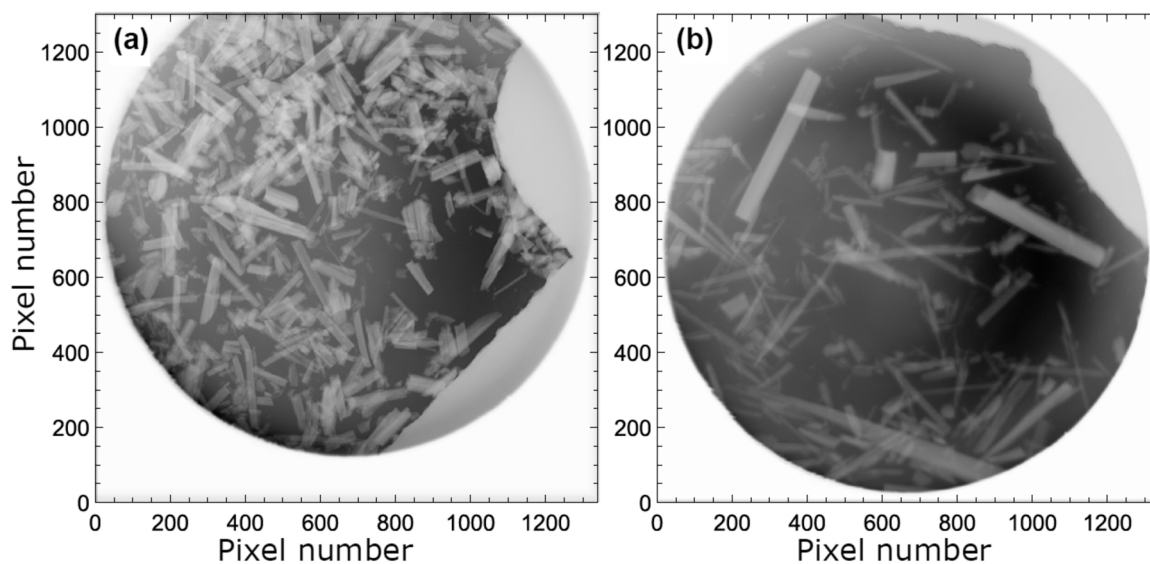

Fig. 10. Spatially resolved intensities of transmitted X-rays for a) $MoNi_4/MoO_2$ and b) $NiMoO_4$ samples.

$NiMoO_4$ and $MoO_2/MoNi_4$ samples are clearly distinct. Fig. 9 presents the representative Mo L_3-edge NEXAFS for the $NiMoO_4$ and $MoO_2/MoNi_4$ samples. These spectra reflect the transition from Mo(2p) to Mo (4d) electronic states. For the metal oxides, they are sensitive to the oxidation state of Mo (Liu and Li, 2016). The splitting of Mo-L_3 features is caused by the metal-ligand interaction and indicates the splitting of the Mo(4d) orbitals (e_g and t_{2g}), caused, in turn, by the symmetry of the crystal structures. The electronic density of states (band structure) of the studied components results in significant differences in the NEXAFS features as shown in Fig. 9.

The MoL$_3$-edge NEXAFS of $NiMoO_4$ shows a main peak at 2526.0 eV and an additional shoulder at 2524.6 eV. This Mo(4d) orbital splitting of 1.4 eV at the Mo-L_3 edge (the Mo(4d) orbital splitting for a-$NiMoO_4$ with octahedral coordination is > 3.0 eV) and the shape of the peak/shoulder features are indications for tetrahedral coordination (A.A. Bolzan et al., 1995), i.e., the mixed oxide is either hydrated $MoNiO_4$ or α-$NiMoO_4$ (Hao et al., 2015; Rodriguez et al., 1998). XRD data of this sample

confirm that the precursor cuboids crystallized in the hydrate phase $NiMoO_4 \bullet nH_2O$ with a triclinic unit cell (space group P-1) (Zhang et al., 2018), which is different to the monoclinic α and β-$NiMoO_4$ phases existing under atmospheric pressure (space group $C12/m1$) (de Moura et al., 2015). The Mo L_3-edge NEXAFS of the other sample ($MoO_2/$-$MoNi_4$) consists of a superposition of spectra generated from MoO_2 (oxidation state 4 +) and $MoNi_4$ (intermetallic compound). The broad peaks at the Mo L_3-edge exhibit no resonance peak, which indicates the superposition of two metal-like spectra from "metallic" MoO_2 and from the intermetallic phase $MoNi_4$ (mainly metallic bonding with ionic contributions). This observation confirms XRD and TEM data of this sample that the Mo oxide investigated is metallic MoO_2, a rutile-like structure with a monoclinic unit cell (space group $P2_1/c$) (Zhang et al., 2017).
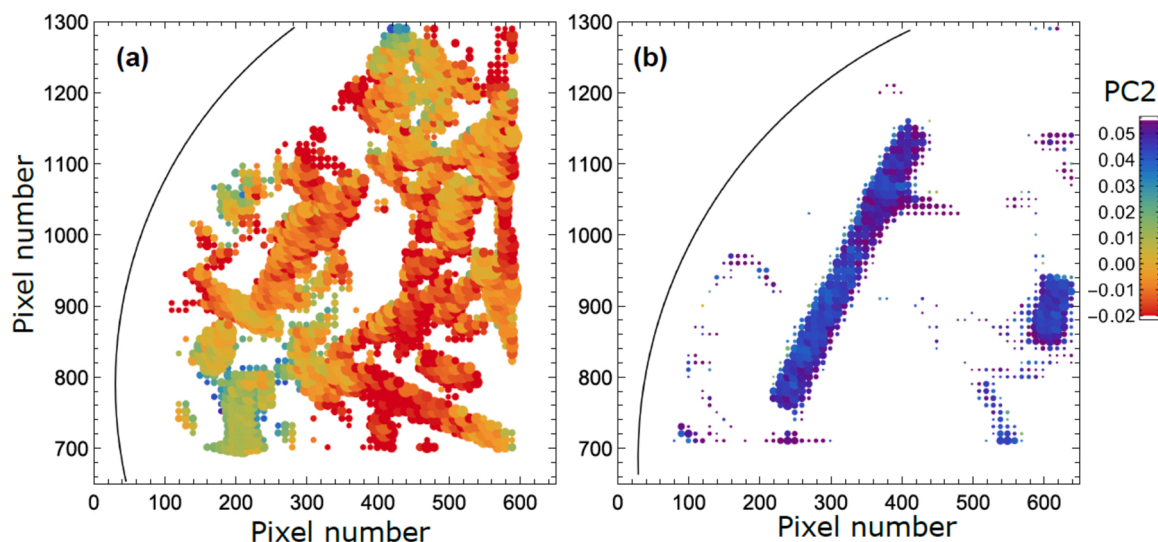
Fig. 11. Identification of Mo species and their concentrations at each pixel for $MoNi_4/MoO_2$ and $NiMoO_4$ samples (from Mo-L_2 edge). The size of the dots corresponds to the relative concentration of Mo atoms at a given pixel (as determined from the jump value of the absorption edge in the X-ray absorption spectra). The color of the dots shows the weight of the 2nd principal component (PC2) in the X-ray absorption spectrum measured at a given pixel.
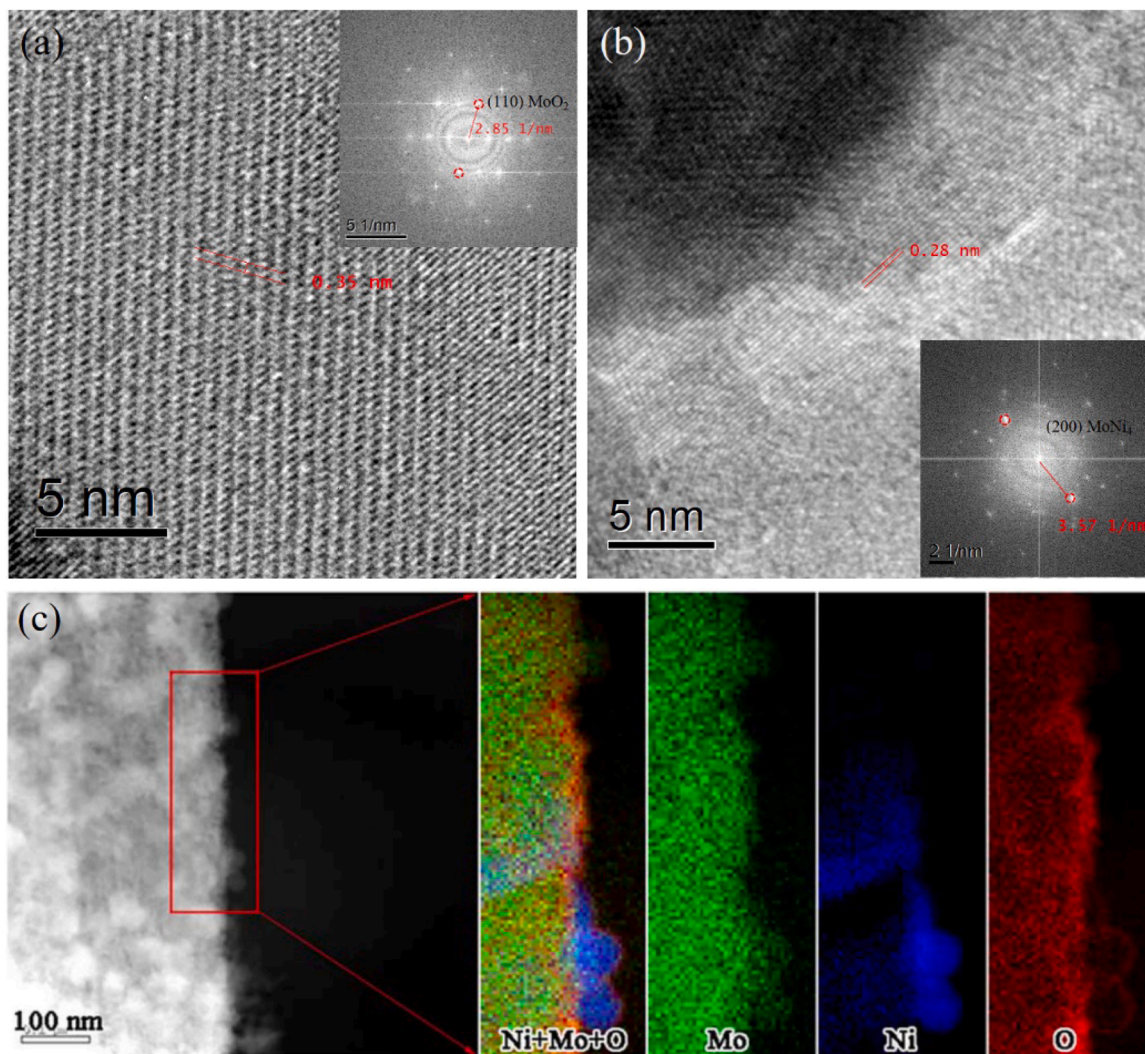

Fig. 12. Analysis of the $MoNi_4/MoO_2$ sample in the TEM. (a)–(b) HRTEM images of $MoNi_4/MoO_2$, the inset images in a and b are the corresponding FFT images; (c) elemental mapping images of the $MoNi_4$ electrocatalysts and the MoO_2 cuboid. Fig. 12 c is adapted from Zhang et al. (2017).

4. Conclusions

Multi-scale tomography is an approach that combines the 3D image information at several hierarchical levels (typical feature sizes of structures). For hierarchically structured complex systems, the combination of techniques and tools that are characterized by different field-of-view (sample volume) and spatial resolution is required for a comprehensive description of the system morphology. Multi-scale 3D imaging using micro and nano XCT, as demonstrated here for a MoNi$_4$/MoO$_2$@Ni composite, provides comprehensive 3D information about the hierarchical structure of the electrocatalyst nondestructively and with high accuracy. This morphology information describes the formed nanostructures, e.g., nanosized particles on supporting structures, and it allows one to increase the total electrochemically active surface area, the number of active catalytic sites, and the ion diffusion (i.e., the reaction rate). In this particular case, size distribution and shape of Mo oxide cuboids and the formation of nano-sized Mo-Ni intermetallic particles are determined (Topal, Liao, et al., 2020). The high accuracy of 3D morphological data of the formed micro- and nanostructures is ensured by applying machine learning algorithms for the correction of imaging artefacts of high-resolution XCT such as beam hardening and for the compensation of experimental inaccuracies such as misalignment and motions of samples and tool components. The used reconstruction software, empowered by machine learning algorithms, significantly improves the reconstruction quality of the acquired data for both micro-XCT using cone-beam geometry and nano-XCT using parallel-beam geometry (Topal, Loeffler, et al., 2020).

The morphology information is of particular interest for the up-scaling of processes and for the development of technologies to fabricate advanced energy conversion devices. Tomography studies, both electron and X-ray, at different scales and with different spatial resolutions, allow to develop, optimize and control the electrocatalytic processes in devices, particularly substrate and precursor as well as process temperature and time. These parameters have to be balanced to achieve an optimal hierarchical morphology of the electrochemical system, i.e., that the formed nanosized particles will guarantee an efficient and durable operation during the requested lifetime of an energy conversion device. Particularly, size distribution and shape of cuboids and the formation of nano-sized particles can be controlled. Special nanostructures (e.g., arrangements of nanoparticles with optimized size distribution and porous films) can be developed and characterized to avoid chemical leaching of active species.

The high electrocatalytic efficiency of Mo-Ni-based alloy (Mo$_x$Ni$_y$) electrocatalysts for the hydrogen evolution reaction (HER) is based on their advantageous crystalline structure and chemical bonding. That means, complementary to the 3D morphology data, information about the surface chemistry, i.e., the crystalline structure of the materials and the chemical bonding, is needed to improve specific surface properties. High-resolution TEM images and selected-area electron diffraction patterns, supported by X-ray diffraction (XRD), reveal the crystalline structures of Mo-based oxides and MoNi$_4$. The extension of the photon energy range into the tender X-ray range up to about 3 keV (at a synchrotron radiation source) allows measuring the Mo-L NEXAFS spectra, which is not possible with EELS in the TEM since the ionization energy is too high for the acquisition of an ionization edge with sufficient intensity. Mo-L NEXAFS spectromicroscopy is a suitable technique to identify the 4d transition metal oxides based on their electronic structures and the valence states of the metal ions for nanostructured electrocatalytic systems. Principal component analysis (Wasserman, 1997) provides the chemical states for the investigated components of an electrocatalyst. In this particular case it was proven that the temperature-time dependent Ni out-diffusion process to form the electrocatalytically active MoNi$_4$ nanoparticles was fully completed.

Specially designed operando studies in laboratory tools, such as TEM and XCT, will provide information about kinetics processes, i.e., the transition of NiMoO$_4$ cuboids into MoO$_2$ cuboids and the formation of the nanosized Mo-Ni particles. In addition, degradation processes during operation of catalytic systems, particularly anode electrocatalyst operation at high current density that increases both cell potential and temperature and that causes significant durability issues, can be studied using operando chambers in microscopes that allow one to vary pH value, electrode potential and temperature systematically. In particular, the anodic oxygen evolution reaction is the determining step for the degradation rate of the entire process, and it affects significantly the system stability. We believe that our multi-scale tomography study of the 3D morphology of electrocatalysts will open up a new exciting avenue toward exploring the design of robust 3D electrocatalysts with high activity and durability for large-scale hydrogen production.

Declaration of Competing Interest

The authors declare that they have no known competing financial interests or personal relationships that could have appeared to influence the work reported in this paper.

Acknowledgments

References

ANSYS SpaceClaim, 2019. ANSYS Inc., Canonsburg, PA, USA.

Bolzan, A., Kennedy, B., Howard, C., 1995. Neutron powder diffraction study of molybdenum and tungsten dioxides. Aust. J. Chem. 48, 1473–1477.

Bolzan, A.A., Kennedy, B.J., Howard, C.J., 1995. Neutron powder diffraction study of molybdenum and tungsten dioxides. Aust. J. Chem. 48, 1473–1477.

Egerton, R.F., 2011. Electron Energy-Loss Spectroscopy in the Electron Microscope, 3rd ed. Springer.

Feldkamp, L.A., Davis, L.C., Kress, J.W., 1984. Practical cone-beam algorithm. J. Opt. Soc. Am. A 1, 612.

Hao, J., Yang, W., Zhang, Z., Tang, J., 2015. Metal-organic frameworks derived Co$_x$Fe$_{1-x}$P nanocubes for electrochemical hydrogen evolution. Nanoscale 7, 11055–11062.

Inzani, K., Nematollahi, M., Vullum-Bruer, F., Grande, T., Reenaas, T.W., Selbach, S.M., 2017. Electronic properties of reduced molybdenum oxides. Phys. Chem. Chem. Phys. 19, 9232–9245.

Lajaunie, L., Boucher, F., Dessapt, R., Moreau, P., 2015. Quantitative use of electron energy-loss spectroscopy Mo-M$_{2,3}$ edges for the study of molybdenum oxides. Ultramicroscopy 149, 1–8.

Liu, M., Li, J., 2016. Cobalt phosphide hollow polyhedron as efficient bifunctional electrocatalysts for the evolution reaction of hydrogen and oxygen. ACS Appl. Mater. Interfaces 8, 2158–2165.

de Moura, A.P., de Oliveira, L.H., Rosa, I.L.V., Xavier, C.S., Lisboa-Filho, P.N., Li, M.S., La Porta, F.A., Longo, E., Varela, J.A., 2015. Structural, optical, and magnetic properties of NiMoO$_4$ nanorods prepared by microwave sintering. Sci. World J. 315084.

Radon, J., 1986. On the determination of functions from their integral values along certain manifolds. IEEE Trans. Med. Imaging 5, 170–176.

Rodriguez, J.A., Chaturvedi, S., Hanson, J.C., Albornoz, A., Brito, J.L., 1998. Electronic properties and phase transformations in CoMoO$_4$ and NiMoO$_4$: XANES and time-resolved synchrotron XRD studies. J. Phys. Chem. B 102, 1347–1355.

Scanlon, D.O., et al., 2010. Theoretical and experimental study of the electronic structures of MoO$_3$ and MoO$_2$. J. Phys. Chem. C 114, 4636–4645.

Simpleware ScanIP, 2019. Synopsys, Inc., Mountain View, CA, USA.

Topal, E., Loeffler, M., Zschech, E., 2020. Deep learning-based inaccuracy compensation in reconstruction of high resolution XCT data. Sci. Rep. 10, 7682.

Topal, E., Liao, Z., Loeffler, M., Gluch, J., Zhang, J., Feng, X., Zschech, E., 2020. Multi–scale X–ray tomography and machine learning algorithms to study MoNi$_4$ electrocatalysts anchored on MoO$_2$ cuboids aligned on Ni foam. BMC Mater. 2, 5.

Vij, V., Sultan, S., Harzandi, A.M., Meena, A., Tiwari, J.N., Lee, W.G., 2017. Nickel-based electrocatalysts for energy-related applications: oxygen reduction, oxygen evolution, and hydrogen evolution reactions. ACS Catal. 7, 7196–7225.

Wasserman, S.R., 1997. The analysis of mixtures: application of principal component analysis to XAS spectra. J. Phys. IV 7 (C2), 203–205.

Werner, S., Rehbein, S., Siewert, F., Sokolov, A., Mast, M., Huang, Q., Feng, Y., Li, T., Senf, F., Follath, R., Liao, Z., Kutukova, K., Zhang, Jian, Feng, Xinliang, Wang, Z., Zschech, E., Guttmann, P., Schneider, G., 2022. Closing the tender photon energy gap for nanoscale X-ray spectromicroscopy. Light (submitted for publication).

Xu, M., Han, L., Han, Y., Yu, Y., Zhai, J., Dong, S., 2015. Porous CoP concave polyhedron electrocatalysts synthesized from metal–organic frameworks with enhanced electrochemical properties for hydrogen evolution. J. Mater. Chem. A 3, 21471–21477.

Zhang, J., Wang, T., Liu, P., Liao, Z., Liu, S., Zhuang, X., Chen, M., Zschech, E., Feng, X., 2017. Efficient hydrogen production on $MoNi_4$ electrocatalysts with fast water dissociation kinetics. Nat. Commun. 8, 15437.

Zhang, Y., Xiao, J., Lv, Q., Wang, S., 2018. Self-supported transition metal phosphide based electrodes as high-efficient water splitting cathodes. Front. Chem. Sci. Eng. 12, 494–508.